

The role of etching anisotropy in the fabrication of freestanding oxide microstructures on $\text{SrTiO}_3(100)$, $\text{SrTiO}_3(110)$, and $\text{SrTiO}_3(111)$ substrates

Alejandro Enrique Plaza,¹ Nicola Manca,^{1, a)} Cristina Bernini,¹ Daniele Marré,^{2, 1} and Luca Pellegrino¹

¹⁾CNR-SPIN, C.so F. M. Perrone, 24, 16152 Genova, Italy

²⁾Dipartimento di Fisica, Università degli Studi di Genova, 16146 Genova, Italy

The release process for the fabrication of freestanding oxide microstructures relies on appropriate, controllable and repeatable wet etching procedures. SrTiO_3 is among the most employed substrates for oxide thin films growth and can be decomposed in HF:water solution. Such process is strongly anisotropic and is affected by local defects and substrate cut-plane. We analyze the etching behavior of SrTiO_3 substrates having (100), (110), and (111) cut-planes during immersion in a 5% HF:water solution. The etching process over the three substrates is compared in terms of pitting, anisotropy, macroscopic etch rate and underetching effects around HF-resistant $(\text{La,Sr})\text{MnO}_3$ thin film micropatterns. The release of targeted structures, such as the reported $(\text{La,Sr})\text{MnO}_3$ freestanding microbridges, depends on the substrate crystallographic symmetry and on the in-plane orientation of the structures themselves along the planar directions. By comparing the etching evolution at two different length scales, we distinguish two regimes for the propagation of the etching front: an intrinsic one, owing to a specific lattice direction, and a macroscopic one, resulting from the mixing of different etching fronts. We report the morphologies of the etched SrTiO_3 surfaces and the geometries of the underetched regions as well as of the microbridge clamping zones. The reported analysis will enable the design of complex MEMS devices by allowing to model the evolution of the etching process required for the release of arbitrary structures made of oxide thin films deposited on top of STO.

This article may be downloaded for personal use only. Any other use requires prior permission of the author and AIP Publishing. This article appeared in "A. Plaza *et al.*, Appl. Phys. Lett. 119, 033504, (2021)" and may be found at <http://dx.doi.org/10.1063/5.0056524>

SrTiO_3 (STO) is a standard substrate for the deposition of many transition metal oxides (TMO) thin films¹ and for the realization of oxides-based devices due to its convenient lattice parameter, variety of surface preparation procedures, wide band gap, and large dielectric constant² and, recently, it has been employed as preferential substrate for developing new oxide MEMS devices³⁻⁹ without requiring integration procedures with Si technology.¹⁰⁻¹⁵ Common commercially available SrTiO_3 substrate crystal cuts are (100), (110) and (111). STO(100) is the most studied and used one, it is weakly polar and has the highest surface symmetry. In contrast, STO(110) and STO(111) crystal cuts are polar and have a reduced in-plane symmetry that makes them prone to surface reconstructions and adsorbates that influence device fabrication steps.¹⁶⁻¹⁸ The proposed etching model of single-crystal SrTiO_3 is the so-called "Dislocation hierarchical tree structure",¹⁹ which takes into account both rate dispersion and induced surface morphology and many critical details of this behavior have been tested so far.²⁰⁻²² A complementary concept to this crystallographic approach is the "Reactive surface area", associated to methods suitable to study the variability of etch rates and mechanisms on a bigger scale.²³⁻²⁵ Notwithstanding the significative overall results briefly reviewed, SrTiO_3 specific results regarding crystal cut, anisotropy and etch rate variability in the case of MEMS

fabrication are still lacking. In such a case, many parameters are fixed due to device specification constraints. Hence, the specific effects of crystal cut and device orientation, are very relevant. In order to develop a MEMS technology based on crystalline oxide thin films deposited on top of SrTiO_3 substrates, it is thus crucial to understand the evolution of the substrate etching process along different lattice directions, in particular with respect to the planned device geometry and feature size.

In this work, we analyze faceting, etch rates, pitting and underetching effects of chemically etched (5% HF aqueous solution) STO substrates having different cut-planes, namely (100), (110), and (111). We employ $5 \times 5 \times 0.5 \text{ mm}^3$ single crystal substrates from CrysTec GmbH with miscut angle below 0.1° . We compare the etching evolution on two different device geometries designed to measure both the STO etching rates at the macroscale and the etching dynamics at the microscale. For the former, we use a hard mask made from a 50 nm thick $(\text{La}_{0.7}\text{Sr}_{0.3})\text{MnO}_3$ (LSMO) film with $200 \times 200 \mu\text{m}^2$ square holes array. For the latter, we investigate the under-etching and the release process of 100 nm thick and $5 \mu\text{m}$ wide LSMO microbridges.

LSMO films are grown by Pulsed Laser Deposition (PLD) from a sintered powder target using an excimer laser (248 nm wavelength) having beam energy density of 0.6 J/cm^2 and 2 Hz repetition rate. The deposition temperature is 800°C and the oxygen background pressure 10^{-4} mbar. After the growth, the films are in-situ annealed for 20 minutes at 600°C and 200 mbar of oxygen pressure. Both hard mask and microbridge samples

^{a)}Electronic mail: nicola.manca@spin.cnr.it

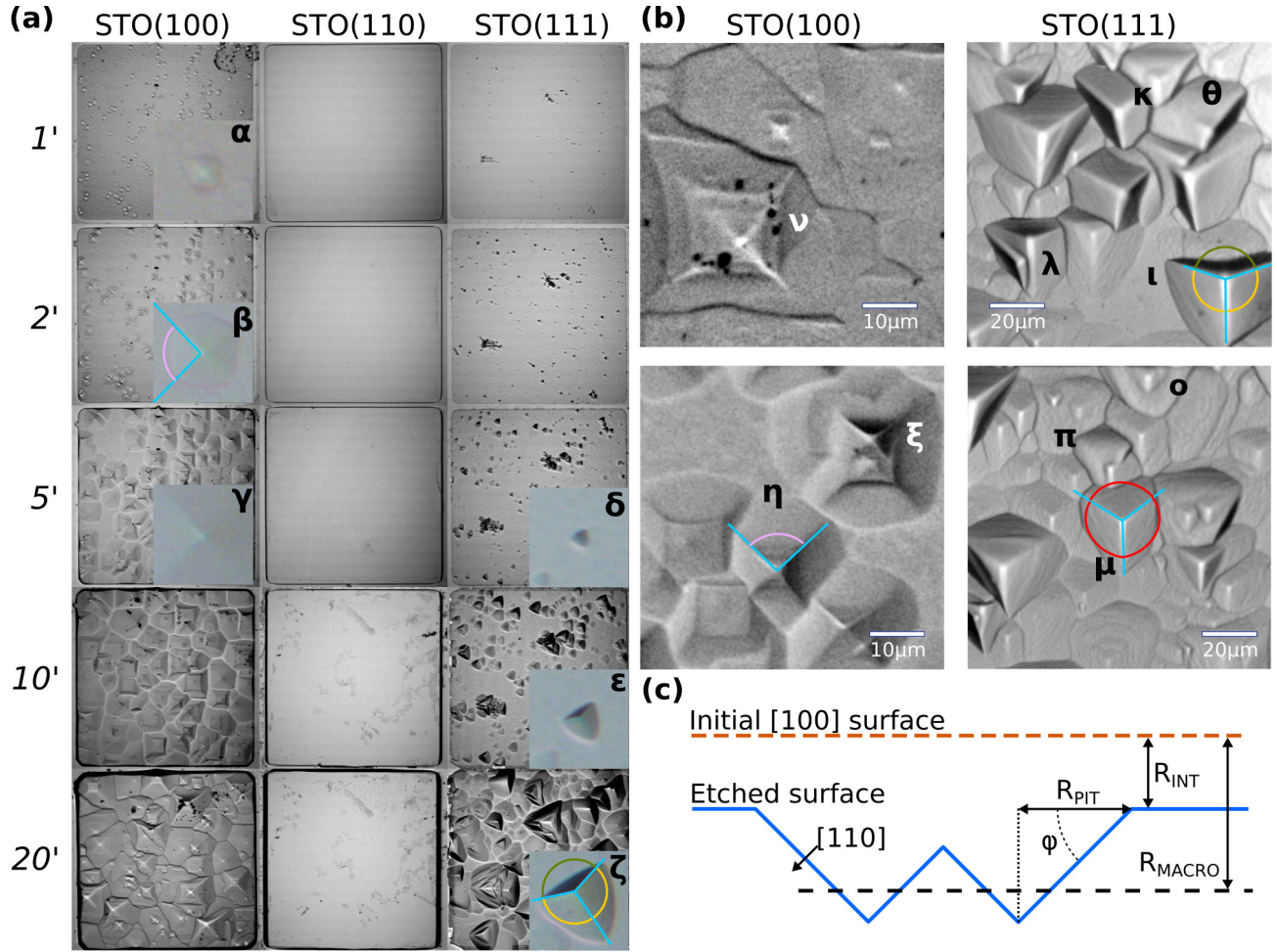


FIG. 1. Optical microscopy images of etched square holes of 200 μm lateral size. (a) Pictures taken at different etching times. Insets are magnified pit details. The visible dark-grey marks on the STO(110) surface are not pits, but residues of strontium fluoride coming from the STO chemical etching process (see Supplementary Material, Sec. I). (b) Details of the etched surface, where the STO(100) pictures were acquired after 5 minutes of etching while the STO(111) ones after 60 minutes. In-plane angles are 90° (pink), 110° (green), 140° (yellow), 120° (red). (c) Simplified illustration of the etching evolution in the out-of-plane direction for a STO(100) substrate.

are fabricated by standard optical lithography as described in previous works from our group.^{3,7} The hard mask etched samples are obtained by put soaking together (100), (110) and (111) STO samples in HF (5% in aqueous solution) kept at 30 °C. This allows us to perform some statistical analysis and test for homogeneity over the sample surface. At given times (1, 2, 5, 10, 20, 40 and 60 minutes), they are all removed from the bath, cleaned in deionized water, dried under nitrogen flow, and inspected at the optical microscope. LSMO microbridges oriented along three in-plane orientations (0°, 45°, and 90°) were realized on three substrates having different cut-planes and fabricated following the same procedure discussed above, with the only difference that after 60 minutes of etching they were dried using a Critical Point Drying system. HF decomposes the STO, leaving water-insoluble salts on the surfaces that are identified as strontium fluoride (see Supplementary Material, Sec. I). The removal of such salts is achieved mechani-

cally during the etching process by magnetic stirring at the relatively slow rotational speed of ≈ 200 r.p.m., so as to avoid the break of the microstructures by drag forces.

We start by discussing the etching process at the macroscale by monitoring two characteristics of the STO substrate regions that are not covered by the LSMO hard mask: (1) the formation, alignment, and evolution of pyramidal etch pits; (2) the overall substrate etching in the out-of-plane direction.

The pits form and progressively grow on the STO(100) and STO(111) substrates, resulting in surfaces covered with well-formed pyramidal pits of quite uniform lateral dimension after 10 min and 40 min for STO(100) and STO(111), respectively (see Figure 1(a)). STO(100) pits have square symmetry with a centered apex as shown in Fig. 1(a) (α , β , γ) and (b)(η), while STO(111) pits have triangular section, with the apex mostly shifted from the symmetry center, as visible from the shadowed bounding plane in Fig. 1(b) (θ , ι , κ , λ) and in some case with

Direction	Method	Rate eq.	RMS	Etchant	Temperature	Reference
[001]	R _{MACRO}	13.5 $\mu\text{m}/\text{h}$	1 μm	5% (2.8M) HF	30°C	This work
[011]	R _{MACRO}	9 $\mu\text{m}/\text{h}$	4 nm	5% (2.8M) HF	30°C	This work
[111]	R _{MACRO}	0.6 $\mu\text{m}/\text{h}$	0.75 μm	5% (2.8M) HF	30°C	This work
[001]	Surface	1.2 $\mu\text{m}/\text{h}$	N/A	2.5M HF	30°C	Ref. 26
[001]	Pits depth	11.1 $\mu\text{m}/\text{h}$	N/A	2.5M HF	30°C	Ref. 26
[001]	Pits depth	21.6 $\mu\text{m}/\text{h}$	N/A	N/A	N/A	Calculated from Ref. 19
[001]	Terraces	0.01 $\mu\text{m}/\text{h}$	N/A	Buffered HF	“Room Temperature”	Calculated from Ref. 27
[011]	Surface	6.0 $\mu\text{m}/\text{h}$	N/A	2.5M HF	30°C	Ref. 26
[001]	R _{PIT}	5 $\mu\text{m}/\text{min}$	N/A	5% (2.8M) HF	30°C	This work
[111]	R _{PIT}	1.3 $\mu\text{m}/\text{min}$	N/A	5% (2.8M) HF	30°C	This work

TABLE I. Comparison etching rate for SrTiO₃ single crystal in HF bath along the [001], [011], and [111] directions. In our work the etch front rate is calculated by considering the final depth after 60 mins. The RMS evaluates the surface roughness and is calculated over the entire 200×200 μm^2 square mask (see also the Supplementary Material, Sec II and III). For an in-depth comparison a particular care with respect to how the rate is defined in each of the referenced works is required.

a remarkable symmetry, as in Fig. 1(b) (μ). For both STO(100) and STO(111) substrates, the pits bounding planes are parallel to (hh0) substrate planes and all the pits are identically oriented with respect to the substrate. As the etching proceeds, already existing pits grow in size, but nucleation of new pits is not observed over the pristine STO surface. During pit growth, other localized events can be found that are able to change pit bounding planes direction, as in Fig. 1(b) (λ), or even the pit morphology (i.e. a pyramidal pit within a flat pit), as in Fig. 1(b) (ν, η, π, ϕ). By following the evolution of individual pits, as shown in Fig. 1(a) (α, β, γ) and (δ, ϵ, ζ), it is possible to estimate their in-plane growth rate (R_{PIT} of Fig. 1(c)), reported in Table I, as long as they do not coalesce. The indicated growth rates are in agreement with literature²⁶. Finally, once the surface is cluttered with overlapping pits, the etching proceeds distributed all over the exposed substrate surface. In contrast, the STO(110) substrate remains pretty flat even at the end of the etching process, with a r.m.s. roughness of about 4 nm, as measured by AFM, and no detectable pit formation (see Supplementary Material, Sec. II). Such striking difference shows, in accordance with previous literature reports, that the [110] direction is a fast etching direction, since no pit eventually nucleated on this face would be able to survive on its own.²⁶

As schematically illustrated in Fig. 1(c) (showing the STO(100) case), the overall out-of-plane etching rate on a large scale (several tens of micrometers) is a combination of different processes, also including the evolution of the pits. In fact, the etch front along a direction (intrinsic rate R_{INT}) given by a crystallographic face may proceed by the removal of crystalline layers in the same crystallographic direction or by removing layers in different and faster etching directions, enhancing the overall etching rate through the formation of pits (in plane pit growth rate R_{PIT}). Moreover, during the pitting process, a flat surface along a slow etching direction may form (i.e. truncated pyramidal pits) decreasing the etching speed unless new pits are formed. Considering these mechanisms, the nucleation and the growth of different etching planes may depend on local conditions (i.e.

etchant concentration gradients, local fluid velocity, salt precipitation and contamination, etc.). However, taking into account that the observed pit characteristic length is well below the size of the exposed regions in our hard mask, we can evaluate the average large-area etching (R_{MACRO}) rate for STO(100), STO(110) and STO(111) substrates by inspecting our samples after 60 minutes of etching. This was performed by an optical profilometer (see Supplementary Material, Sec. III), and the results of this analysis are reported in Table I, together with a comparison with etching rates reported in previous works.

A second important aspect, directly related to the release process of suspended microstructure, is the evolution of the underetch profile, i.e. the STO region etched below the mask at the edges of patterned structures. We now analyze the evolution of the underetching below the LSMO microbridge and the geometry of the underetch profile around the LSMO microbridge clamping regions for different substrate types and microbridge directions.

In Figure 2 and Figure 3 suspended regions appear as light-gray colored and progressively evolve around all the borders of the LSMO patterns. The optical inspection (Fig. 2) monitors the 2D projection of the underetch profiles only, while their tridimensional structure is better evidenced in the SEM pictures reported in Fig. 3. In the following, in-plane directions are defined as ‘ x' ’, ‘ y' ’ and ‘ xy' ’, corresponding to the substrate edges and diagonal, respectively, while ‘ z' ’ is the out-of-plane direction, as indicated in Fig. 2(a). In the STO(100) the extension of the underetched region is similar in both the equivalent directions x and y (Fig. 2(b) (α, β, γ)), but smaller for bridges oriented along the xy direction (Fig. 2(b) (γ)). STO(110), instead, presents a less symmetric pattern with a straight underetch profile in the y direction, characterized by vertical walls (Fig. 2(b) (δ) and Fig. 3(c). This is in contrast with the rough underetch profile in x and xy directions (Fig. 2(b) (ϵ), and Fig. 3(d). For the STO(111) case, the underetch profile is characterized by a larger extension below the LSMO pattern and a marked asymmetry between the $+x$ and $-x$ directions, as evidenced in Fig. 2(b) (ζ). The etching in the z direc-

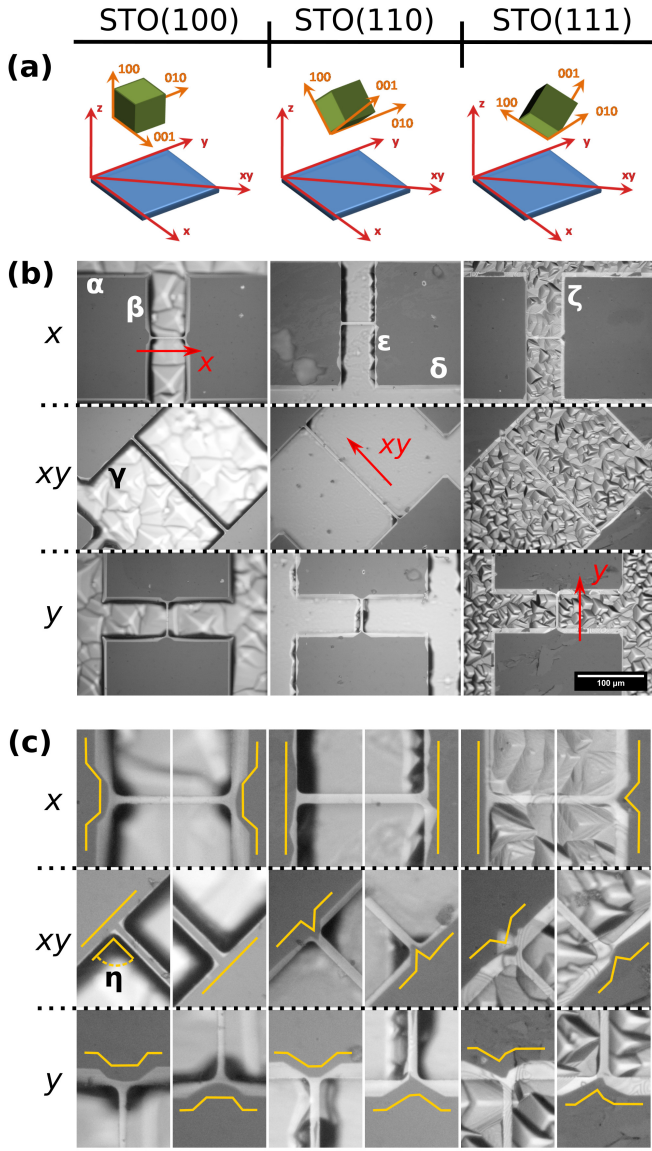


FIG. 2. (a) Scheme of the experiment, indicating the three STO samples and crystallographic directions: STO substrate surface (blue); sample directions (red); crystal unit cell (red); crystal basis directions (orange). (b) Optical microscopy at 40X magnification after 40 minutes etching time of LSMO microbridges of different orientations (rows) on STO substrates with different crystal cut (columns). (c) Magnified detail of the clamping zone of microbridges (Profile sketch in red). Light grey regions are freestanding.

tion is limited and characterized by a faceted surface, as already discussed and visible in Fig. 3(f). The faceted STO underetch profile have different orientations with respect to the bounding planes observed on pits forming in open regions of the substrates (Fig. 3); this fact is a clear indication that geometric boundary conditions significantly contribute in determining the final clamping profile of the etched structures.

The time required to obtain a complete release from the substrate depends on the device geometry and size.

As a general reference, we can consider the reported structures, i.e. 5 μm -wide LSMO microbridges, etching time to be about 30 minutes for all the cases except the two combinations: STO(100) xy -aligned and STO(110) y -aligned. In such cases, etching times exceeding 1 h could be required depending on local defects. Considering these etching times, in general, the underetch profile is not the equilibrium one, as predicted by the Wulff-Jaccodine construction.²⁸ Instead, the profile is determined by the system anisotropy and varies, among other factors, with the in-plane orientation of the pattern, crystal cut-plane and etching time.

Regarding the etching at the clamping zones, the process proceeds even after the microbridge is suspended. The precise geometry of the clamping regions and the symmetry between the two edges of the bridges is discussed in Fig. 2(c). They depend on microbridge orientation and substrate crystal cut as follows:

- STO(100): the clamping region is symmetric for all the three microbridge orientations x , y and xy . In the case of the x and y -oriented microbridges, the clamping zone has a polygonal shape, while in those oriented in the xy direction it has a net flat shape that progressively evolves towards a complete release of the microbridge.
- STO(110): the geometry of the clamping region, although symmetric in both cases, differs significantly between the x and y directions. For x -aligned microbridges, it is flat and aligned with the borders of the pads, while for y -aligned microbridges it protrudes from the pads, outlining a polygon. This is not the case for STO(110) xy -oriented micro-bridges, where asymmetry arises.
- STO(111): a varied mix of shapes and symmetries at the clamping regions can be observed. Microbridges aligned in the x direction have symmetric clamping regions, but one with a flat profile and the other with protruding profile. Microbridges aligned along the y and xy directions have asymmetric clamping regions, with the former showing larger under-etch.

In the following, we show that the complex faceting observed in the clamping regions results from the interplay between substrate cut-planes, device geometry, and anisotropic etching. In addition, at small scales the etching rate measured along different cut planes (nearby pattern features) is different from what extracted from the macroscopic rates R_{MACRO} measured reported in Table I, where the averaging effects over different crystallographic directions plays a major role. This also indicates that the relevant length scale determining the geometry of the edges in micrometric devices is below the threshold required to observe the large-area rates.

The symmetric underetching behavior for STO(100) and the similarity between the x and y directions reflects the crystallographic equivalence between [001]

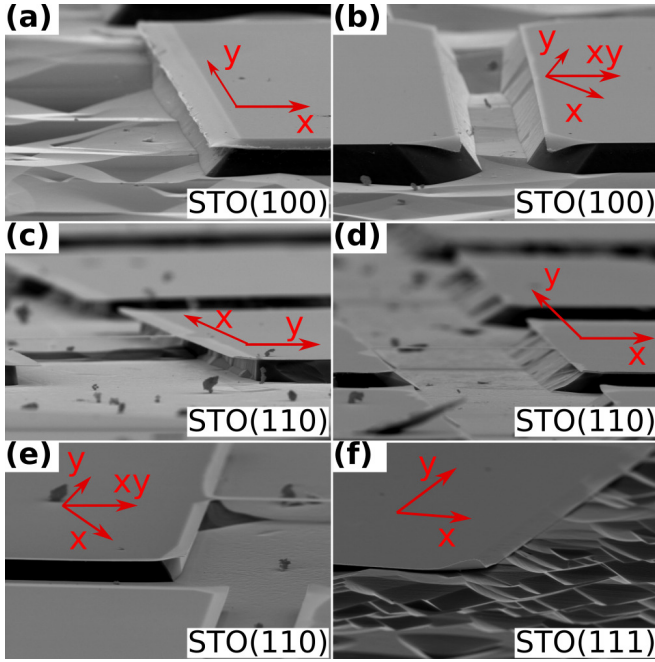


FIG. 3. SEM images of LSMO microbridges between square pads. In-plane directions are reported in red color.

and $[010]$ directions. The lower underetch along xy corresponding to the $[011]$ direction, can be explained considering that this is a fast etching direction, the xy oriented microbridges progressively exhibit walls parallel to the $[1\bar{1}h]$ directions that have a slower etching rate than the pure $[011]$ and $[001]$ ones. The trapezoidal-shaped (in-plane) clamping zones is the result of the $[111]$ face etching that is slower than the $[110]$ face one, hence prevailing the concave corner.²⁸ The 90° angle between the underetch profiles (fig. 2(c) (η)) observed in the clamped regions for the microbridges aligned along the xy direction can be explained considering the formation of underetch faces oriented along equivalent $[111]$ directions. The profile symmetry is guaranteed by the crystallographic equivalence between the involved directions on both sides of the same clamping zone.

The STO(110) underetch in-plane asymmetry arises from the fact that the x and y directions are aligned along the slow $[100]$ and the fast $[110]$ etching directions, respectively. The flat clamping zone of x -aligned microbridges is the result of reaching a steady state condition with the exposure of the (100) faces, which have a slower etching rate. The faceting of the profile observed around the clamping regions along the y direction results from the faceting vicinal to the $[110]$ direction, which determines deep trenches into the substrate along the y -directed border regions. The clamping regions of y -aligned microbridges have a completely different shape, because in this case the underetch vertical walls are the steady state slow-etching faces ($[100]$ equivalent directions). In this case, other residual crystallographic planes are exposed, such as the $[111]$. The symmetry of the clamping regions in both x and y aligned micro-

bridges is due to the fact that, contrary to xy -aligned microbridges, sagittal planes containing microbridges axis are symmetry planes of the crystal lattice.

STO(111) has in-plane crystallographic trigonal symmetry that does not match the symmetry of the microbridge patterns, leading to a variety of clamping zone shape. Due to the lower etch rate in the z direction and the relevant in-plane underetch, it is difficult to measure the extension of the underetch profile. However, by applying the same analysis used for both STO(100) and STO(110), we may argue that microbridges aligned along the x direction have one flat clamping zone probably limited by the slow etching $[100]$ face, while the other clamping region, with a protruding profile, is limited by the equivalent $[010]$ and $[001]$ directions. The y -aligned microbridges clamping regions have asymmetric profiles and are probably limited by the slow etching rate along the $[010]$ and $[001]$ directions in one side and by the fast etching rate along the $[110]$ and $[101]$ on the other side of the microbridge. In the case of xy -aligned microbridges, analogous analysis leads to infer that the clamping regions are limited by slow etching rate along the $[010]$ and $[001]$ directions, each one at different angle with the microbridge sagittal plane, resulting in an asymmetrical profile.

Finally, in order to demonstrate the design opportunity enabled by our study, we show in the Supplementary Material Sec. IV the realization of a LSMO micro-mechanical bridge resonator that can be measured optically by focusing a laser through a double-polished $\text{SrTiO}_3(110)$ substrate. This was made possible thanks to the low RMS of the bottom surface, which is preserved after the chemical etching, and the transparency of SrTiO_3 to visible light. Such configurations will allow to couple TMO-based resonators in proximity to other systems while maintaining an optical readout scheme.

In conclusion, we showed that the choice of the STO crystal cut-plane has significant effects in terms of etching rate, pitting of large areas, microbridge release time, underetching and shape of the clamping regions. With the shrinking of the device size, the presence of pits and their size become increasingly important and, for increasing complexity of MEMS geometries, achieving desired morphology of the released structures will require trade-off solutions based on choosing the proper crystal cut. Lattice defects play also a crucial role in the propagation of the etching front and their statistical spatial distribution determines a critical scale separating large and small-area behavior of the etching process. Moreover, the in-plane orientation of the microbridges has considerable implications on the final geometry of the clamping regions, likely affecting its mechanical behavior. Below we provide few general considerations summarizing the behavior of STO substrates having different cut-planes with respect to the investigated chemical etching process. As a general reference, the lattice symmetry of the substrate is the main characteristic determining how freestanding regions are released and this

should be taken into account for oxide MEMS design.

- STO(100) shows 90° in-plane symmetry and the fastest macroscopic etching direction along the out-of-plane direction and good in-plane etching rates.
- STO(110) shows smooth etched substrate surfaces and good out-of-plane etching rates. It also shows the possibility to obtain sharp underetch walls, taking into account for the device geometry or symmetry.
- STO(111) has the fastest in-plane underetching rate and the lower out-of-plane etching rate

SUPPLEMENTARY MATERIAL

Supplementary material includes the following: SEM image of the deposits of salts scattered over the SrTiO₃ surface and Energy Dispersive X-ray (EDX) spectra; roughness analysis of etched STO(110); optical profilometry images over large-area etched regions; mechanical measurement of a LSMO MEMS through the STO(110) substrate.

ACKNOWLEDGMENTS

We thank Flavio Gatti, Francesco Buatier de Mongeot, and Lorenzo Ferrari Barusso for providing access to the optical profilometer. This work was carried out under the OXiNEMS project (www.oxinems.eu). This project has received funding from the European Union's Horizon 2020 research and innovation programme under grant agreement No 828784.

DATA AVAILABILITY STATEMENT

The data that support the findings of this study are openly available in Zenodo at <http://dx.doi.org/10.5281/zenodo.4738478>.

- ¹D. G. Schlom, L.-Q. Chen, X. Pan, A. Schmehl, and M. A. Zurbuchen, "A Thin Film Approach to Engineering Functionality into Oxides," *Journal of the American Ceramic Society* **91**, 2429–2454 (2008).
- ²A. Biswas, C.-H. Yang, R. Ramesh, and Y. H. Jeong, "Atomically flat single terminated oxide substrate surfaces," *Progress in Surface Science* **92**, 117–141 (2017).
- ³L. Pellegrino, M. Biasotti, E. Bellingeri, C. Bernini, A. S. Siri, and D. Marré, "All-Oxide Crystalline Microelectromechanical Systems: Bending the Functionalities of Transition-Metal Oxide Thin Films," *Advanced Materials* **21**, 2377–2381 (2009).
- ⁴M. Biasotti, L. Pellegrino, E. Bellingeri, N. Manca, A. S. Siri, and D. Marré, "Strain response of La_{0.7}Sr_{0.3}CoO₃ epitaxial thin films probed by SrTiO₃ crystalline microcantilevers," *Applied Physics Letters* **97**, 223503 (2010).
- ⁵C. Deneke, E. Wild, K. Boldyreva, S. Baunack, P. Cendula, I. Mönch, M. Simon, A. Malachias, K. Dörr, and O. G. Schmidt, "Rolled-up tubes and cantilevers by releasing SrRuO₃-Pr_{0.7}Ca_{0.3}MnO₃ nanomembranes," *Nanoscale Research Letters* **6**, 621 (2011).

- ⁶N. Manca, L. Pellegrino, T. Kanki, S. Yamasaki, H. Tanaka, A. S. Siri, and D. Marré, "Programmable Mechanical Resonances in MEMS by Localized Joule Heating of Phase Change Materials," *Advanced Materials* **25**, 6430–6435 (2013).
- ⁷V. Ceriale, L. Pellegrino, N. Manca, and D. Marré, "Electro-thermal bistability in (La_{0.7}Sr_{0.3})MnO₃ suspended microbridges: Thermal characterization and transient analysis," *Journal of Applied Physics* **115**, 054511 (2014).
- ⁸N. Manca, T. Kanki, H. Tanaka, D. Marré, and L. Pellegrino, "Influence of thermal boundary conditions on the current-driven resistive transition in VO₂ microbridges," *Applied Physics Letters* **107**, 143509 (2015).
- ⁹N. Manca, G. Mattoni, M. Pelassa, W. J. Venstra, H. S. J. van der Zant, and A. D. Caviglia, "Large Tunability of Strain in WO₃ Single-Crystal Microresonators Controlled by Exposure to H₂ Gas," *ACS Applied Materials & Interfaces* **11**, 44438–44443 (2019).
- ¹⁰S. H. Baek, J. Park, D. M. Kim, V. A. Aksyuk, R. R. Das, S. D. Bu, D. A. Felker, J. Lettieri, V. Vaithyanathan, S. S. N. Bharadwaja, N. Bassiri-Gharb, Y. B. Chen, H. P. Sun, C. M. Folkman, H. W. Jang, D. J. Kreft, S. K. Streiffer, R. Ramesh, X. Q. Pan, S. Trolier-McKinstry, D. G. Schlom, M. S. Rzchowski, R. H. Blick, and C. B. Eom, "Giant Piezoelectricity on Si for Hyperactive MEMS," *Science* **334**, 958–961 (2011).
- ¹¹D. Le Bourdais, G. Agnus, T. Maroutian, V. Pillard, P. Aubert, R. Bachelet, G. Saint-Girons, B. Vilquin, E. Lefeuvre, and P. Lecoœur, "Epitaxial manganite freestanding bridges for low power pressure sensors," *Journal of Applied Physics* **118**, 124509 (2015).
- ¹²U. K. Bhaskar, N. Banerjee, A. Abdollahi, Z. Wang, D. G. Schlom, G. Rijnders, and G. Catalan, "A flexoelectric microelectromechanical system on silicon," *Nature Nanotechnology* **11**, 263–266 (2016).
- ¹³S. Liu, B. Guillet, C. Adamo, V. M. Nascimento, S. Lebarry, G. Brasse, F. Lemarié, J. El Fallah, D. G. Schlom, and L. Méchin, "Free-standing La_{0.7}Sr_{0.3}MnO₃ suspended micro-bridges on buffered silicon substrates showing undegraded low frequency noise properties," *Journal of Micromechanics and Microengineering* **29**, 065008 (2019).
- ¹⁴Z. H. Lim, M. Chrysler, A. Kumar, J. P. Mauthe, D. P. Kumah, C. Richardson, J. M. LeBeau, and J. H. Ngai, "Suspended single-crystalline oxide structures on silicon through wet-etch techniques: Effects of oxygen vacancies and dislocations on etch rates," *Journal of Vacuum Science & Technology A* **38**, 013406 (2020).
- ¹⁵V. M. Nascimento, L. Méchin, S. Liu, A. Aryan, C. Adamo, D. G. Schlom, and B. Guillet, "Electro-thermal and optical characterization of an uncooled suspended bolometer based on an epitaxial La_{0.7}Sr_{0.3}MnO₃ film grown on CaTiO₃/Si," *Journal of Physics D: Applied Physics* **54**, 055301 (2021).
- ¹⁶P. W. Tasker, "The stability of ionic crystal surfaces," *Journal of Physics C: Solid State Physics* **12**, 4977–4984 (1979).
- ¹⁷F. Sánchez, C. Ocal, and J. Fontcuberta, "Tailored surfaces of perovskite oxide substrates for conducted growth of thin films," *Chem. Soc. Rev.* **43**, 2272–2285 (2014).
- ¹⁸J. Chang, Y.-S. Park, and S.-K. Kim, "Atomically flat single-terminated SrTiO₃ (111) surface," *Applied Physics Letters* **92**, 152910 (2008).
- ¹⁹K. Szot, C. Rodenbücher, G. Bihlmayer, W. Speier, R. Ishikawa, N. Shibata, and Y. Ikuhara, "Influence of Dislocations in Transition Metal Oxides on Selected Physical and Chemical Properties," *Crystals* **8**, 241 (2018).
- ²⁰R. Wang, Y. Zhu, and S. M. Shapiro, "Structural Defects and the Origin of the Second Length Scale in SrTiO₃," *Physical Review Letters* **80**, 2370–2373 (1998).
- ²¹L. Jin, X. Guo, and C. Jia, "TEM study of <110>-type 35.26° dislocations specially induced by polishing of SrTiO₃ single crystals," *Ultramicroscopy* **134**, 77–85 (2013).
- ²²R. Waser, R. Dittmann, G. Staikov, and K. Szot, "Redox-Based Resistive Switching Memories - Nanoionic Mechanisms, Prospects, and Challenges," *Advanced Materials* **21**, 2632–2663 (2009).
- ²³E. Trindade Pedrosa, I. Kurganskaya, C. Fischer, and A. Luttge, "A Statistical Approach for Analysis of Dissolution Rates Including Surface Morphology," *Minerals* **9**, 458 (2019).
- ²⁴A. Luttge, R. S. Arvidson, C. Fischer, and I. Kurganskaya, "Kinetic concepts for quantitative prediction of fluid-solid interactions,"

[Chemical Geology 504, 216–235 \(2019\).](#)

- ²⁵W. H. Casey, M. J. Carr, and R. A. Graham, “Crystal defects and the dissolution kinetics of rutile,” [Geochimica et Cosmochimica Acta 52, 1545–1556 \(1988\).](#)
- ²⁶G. C. Spalding, W. L. Murphy, T. M. Davidsmeier, and J. E. Elenewski, “Faceting of Single-Crystal SrTiO₃ During Wet Chemical Etching,” [MRS Proceedings 587, O6.4 \(1999\).](#)
- ²⁷M. Lippmaa, K. Takahashi, A. Ohtomo, S. Ohashi, T. Ohnishi, N. Nakagawa, T. Sato, M. Iwatsuki, H. Koinuma, and M. Kawasaki, “Atom technology for Josephson tunnel junctions: SrTiO₃ substrate surface,” [Materials Science and Engineering: B 56, 111–116 \(1998\).](#)
- ²⁸R. J. Jaccodine, “Use of Modified Free Energy Theorems to Predict Equilibrium Growing and Etching Shapes,” [Journal of Applied Physics 33, 2643–2647 \(1962\).](#)

Supplementary Material

The role of etching anisotropy in the fabrication of freestanding oxide microstructures on $\text{SrTiO}_3(100)$, $\text{SrTiO}_3(110)$, and $\text{SrTiO}_3(111)$ substrates

Alejandro Plaza,¹ Nicola Manca,^{1,*} Cristina Bernini,¹

Daniele Marré,^{2,1} and Luca Pellegrino¹

¹*CNR-SPIN, C.so F.M. Perrone, 24, 16152 Genova, Italy*

²*Dipartimento di Fisica, Università degli Studi di Genova, 16146 Genova, Italy*

This supplemental material contains the following:

- Section I: SEM image of the deposits of salts scattered over the SrTiO_3 surface and Energy Dispersive X-ray (EDX) spectra.
- Section II: Roughness analysis of etched STO(110)
- Section III: Optical profilometry images over large-area etched regions
- Section IV: Mechanical measurement of a LSMO MEMS through the STO(110) substrate

* nicola.manca@spin.cnr.it

Sec. I. SEM IMAGE OF THE DEPOSITS OF SALTS SCATTERED OVER THE STO SURFACE AND ENERGY DISPERSIVE X-RAY (EDX) SPECTRA

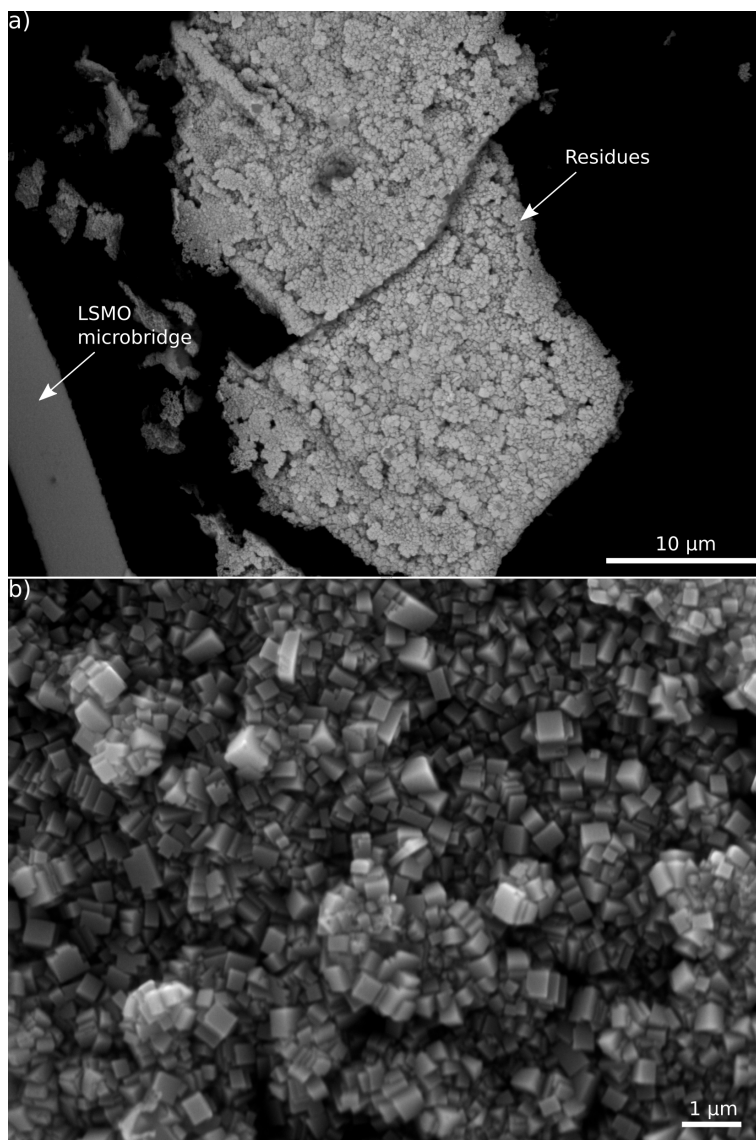


Figure S1. a) Back scattered electron image of deposits observed on the sample surface after chemical etching. b) Secondary electron image of a magnified region of the deposits. Images conditions are: Beam Accelerator Voltage (ETH) 20 kV and working distance 15 mm. These deposits are in great part gradually removed by mild agitation during the etching process. The cubic crystallites are identified as SrF_2 .

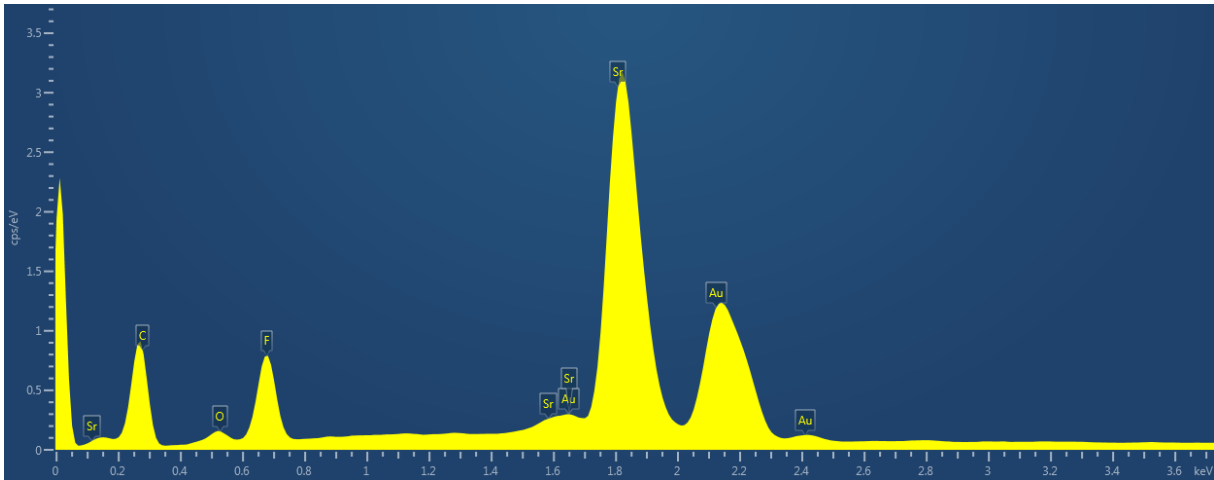


Figure S2. Energy Dispersive X-ray spectrum acquired on the deposits of Figure S1. The sample was prepared by sticking carbon tape over the STO surface and detaching the LSMO microbridges visible in Figure S1(a) and the residues. Strontium and Fluorine are detected. The presence of carbon is justified by the metallization of the sample for SEM measurements, while gold was previously deposited on top of the sample for other characterization purposes.

Element	Line type	Apparent concentration	k Ratio	Wt%	Wt% sigma	Atomic %
F	K series	25.26	0.04959	16.67	0.18	73.15
Sr	L series	27.37	0.24078	28.22	0.21	26.85
Total				44.89		100

TABLE S1. Quantitative analysis of the deposits after the etching of SrTiO_3 in HF 5%

Sec. II. ROUGHNESS ANALYSIS OF ETCHED STO(110)

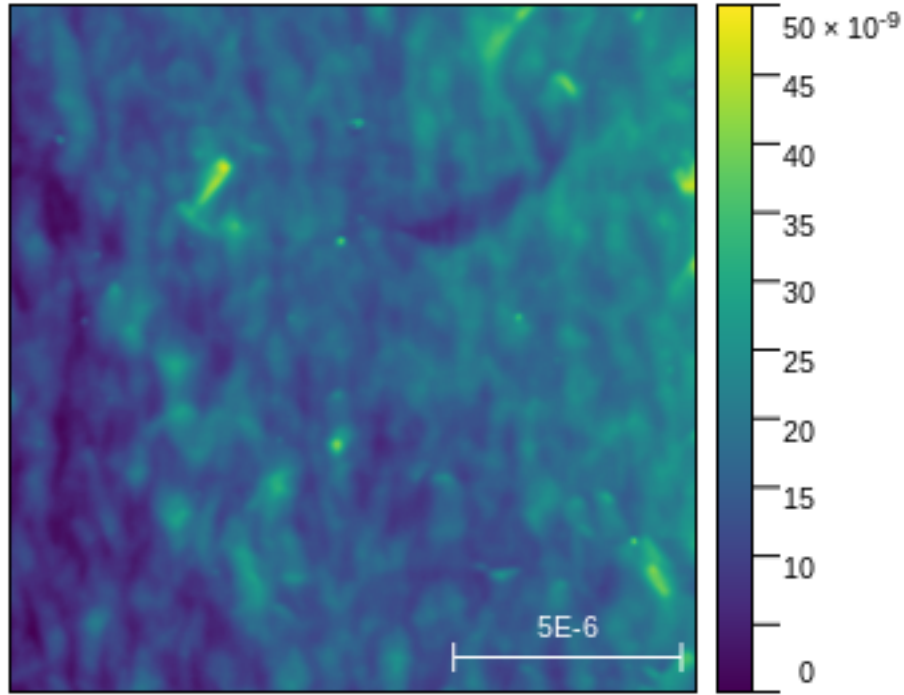


Figure S3. Atomic force microscopy image acquired over a $15 \times 15 \mu\text{m}^2$ area. The surface is a $\text{SrTiO}_3(110)$ sample after 60 minutes of etching in 5% $\text{HF:H}_2\text{O}$ solution. Root-mean-square height value calculated over the whole area is $\approx 4 \text{ nm}$. This image was processed in Gwyddion by performing 2nd-order polynomial background subtraction.

Sec. III. OPTICAL PROFILOMETRY OVER LARGE-AREA ETCHED REGIONS

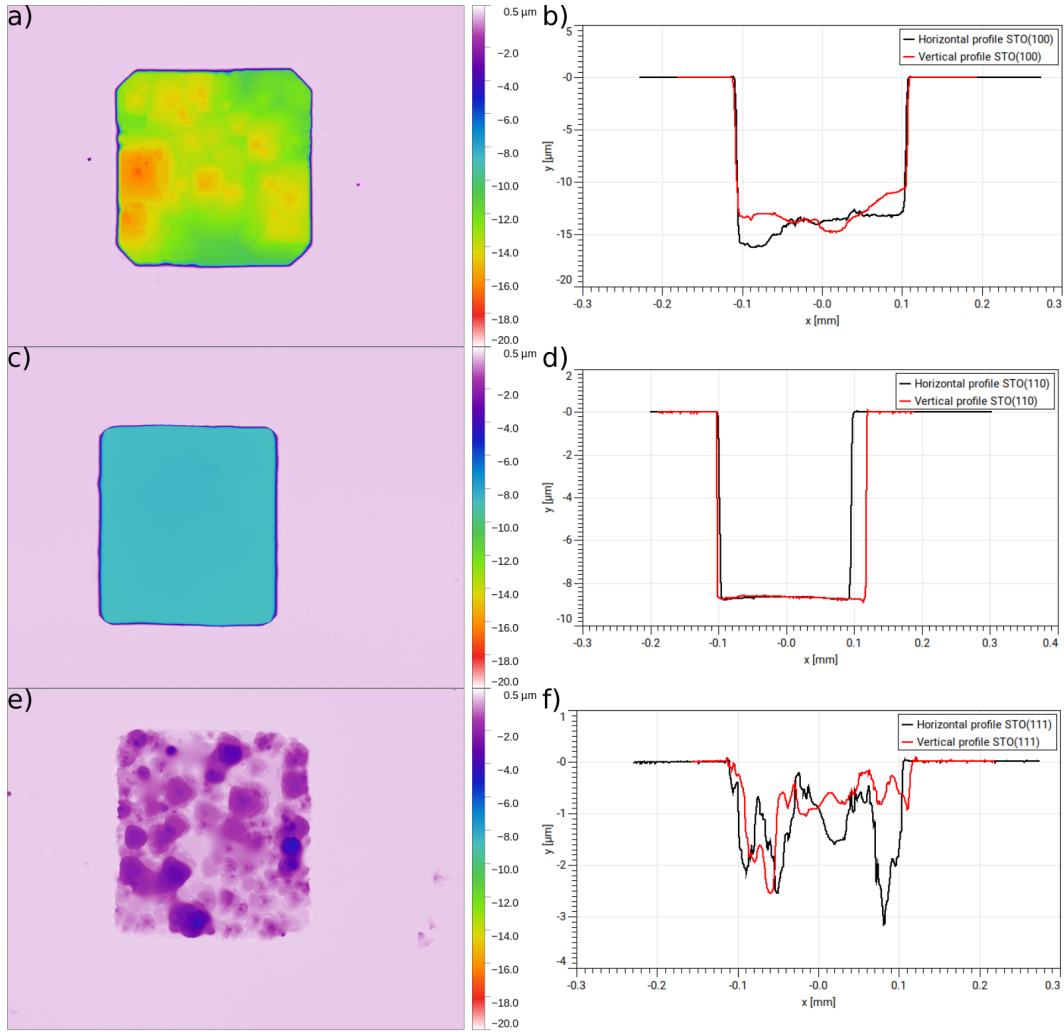


Figure S4. Depth map (left) and profiles line-cut (right) of etched SrTiO₃ (100) (a,b), (110) (c,d), and (111) (e,f) substrates acquired by optical profilometry. The $200 \times 200 \mu\text{m}^2$ squares were patterned using a (La,Sr)MnO₃ hard mask to selectively expose the SrTiO₃ surface. The samples were then put soaking for 1 h in a 5% of HF solution in distilled water. The line profiles were extracted from the central vertical and horizontal axes of the squares. Large-area etch rates and RMS (excluding the RMS for the (110) case) are reported in Table I in the main text and have been calculated from these images by selecting the largest rectangular region comprised within the squares.

Sec. IV. MECHANICAL MEASUREMENT OF A LSMO MEMS THROUGH THE STO(110) SUBSTRATE

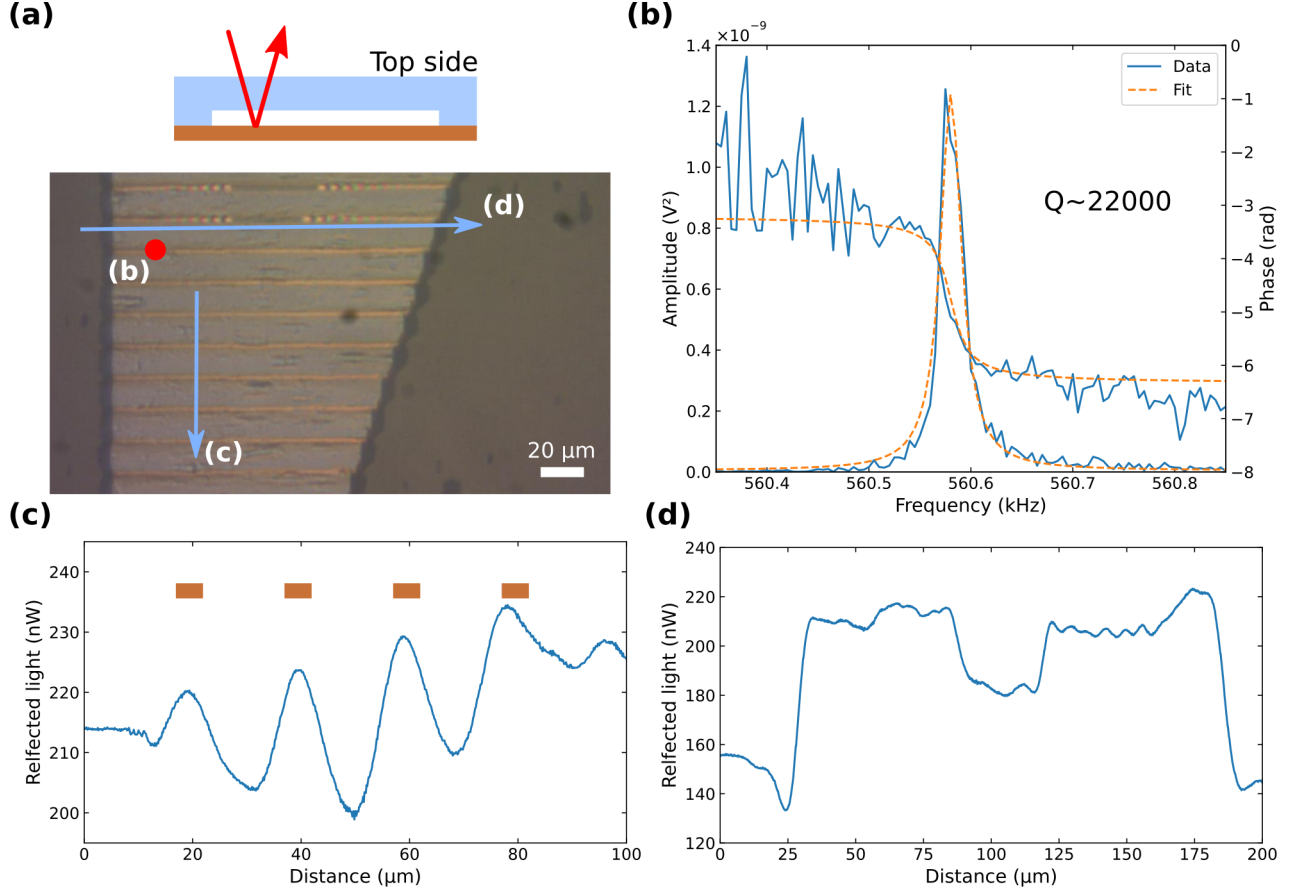


Figure S5. (a) optical microscope image of an array of LSMO suspended microbridges acquired from the backside of a STO(110) double polished substrate. (b) Magnitude and phase (solid blue) together with Lorentzian fit (dashed orange) of the first flexural mode of one of the bridges reported in (a) measured with the laser passing through the substrate. (c)–(d) spatial dependence of the reflected light while moving the laser crossing (c) or along (d) the microbridges' length.

In Figure S5(a) we show a picture in reflected light of an array of 100 nm thick $(\text{La,Sr})\text{MnO}_3$ (LSMO) microbridges fabricated on a 500 μm thick double-polished $\text{SrTiO}_3(110)$ substrate. During the fabrication, the sample was completely immersed in 5% HF solution, with no protective layer on the backside surface. This image is taken from the backside of the substrate and the LSMO microbridges are visible through the transparent substrate itself. Thanks to the etching properties of $\text{SrTiO}_3(110)$ discussed on the main text, the backside SrTiO_3 surface and the SrTiO_3 region below the freestanding LSMO

bridges remain enough flat to allow the focusing of a laser beam directly on the back side of the LSMO microbridge, as schematized in the figure. In Fig. S5(b) we show the measurement of the mechanical resonance of one of the LSMO microbridges presented in (a). The laser beam is focused on the indicated spot in the optical lever geometry and the sample is placed in vacuum (10^{-5} mbar) and at 30 °C. A piezo crystal, glued nearby the sample and connected to a spectrum analyzer, mechanically excites the LSMO microbridges. In Fig. S5(c) we show the spatial dependence of the laser beam power during a scan of the laser beam across different microbridges, as indicated by the vertical blue arrow in (a). The microbridge positions are marked by brown rectangles and correspond to a maximum of the reflected light power. In Fig. S5(d) we perform another similar spatial mapping but during a laser scan along a single microbridge that contacts the substrate at its center. The power of the reflected beam is different in the LSMO film (edges), in the stuck LSMO microbridge (center) and in the freestanding LSMO microbridge regions (intermediate regions). These measurements show that it is possible to conceive a device architecture where the LSMO microbridges are placed in close proximity of an object and perform mechanical characterizations at the same time exploiting the transparency of the substrate of growth.